RESEARCH ARTICLE

Tracking Conical Intersections with Nonlinear X-ray Raman Spectroscopy

Deependra Jadoun and Markus Kowalewski[*]

Department of Physics, Stockholm University, Albanova University Centre, SE-106 91 Stockholm, Sweden.

*Author correspondence to: markus.kowalewski@fysik.su.se

Conical intersections are formed when 2 or more electronic states become degenerate and give rise to ultrafast nonadiabatic processes such as radiation-less decay channels and geometric phase effects. The branching of nuclear wave packets near a conical intersection creates a coherent superposition of electronic states, which carries information about the energy difference of the involved states. X-ray Raman techniques have been proposed to observe the coherent superposition of the electronic states and to monitor the evolving electronic state separation. However, these techniques rely on the coherence generated as the wave packet passes through the conical intersection, and the electronic energy gap before the wave packet passes through the conical intersection is not tracked. In this paper, we theoretically demonstrate how a nonlinear Raman detection scheme can be used to gain further insight into the nonadiabatic dynamics in the vicinity of the conical intersection. We employ a combination of a resonant visible/infrared pulse and an off-resonant x-ray Raman probe to map the electronic state separation around the conical intersection. We demonstrate that this technique can achieve high contrast and is able to selectively probe the narrow electronic state separation around the conical intersection.

Introduction

Many crucial photochemical processes, such as photoisomerization in the primary event of vision [1] and ultraviolet (UV) light-induced DNA damage and repair [2], are mediated by conical intersections (CIs) [3–7]. CIs appear in molecules because of the breakdown of the Born–Oppenheimer approximation (BOA) [8–11] when electronic states are energetically close to each other. The BOA is used to separate the dynamics of electrons and nuclei in a molecule. The electronic and nuclear dynamics become strongly coupled in the vicinity of a CI, which results in an ultrafast and radiation-less population transfer between the involved electronic states. Most polyatomic molecules are believed to exhibit CIs [12], but their direct observation is rather challenging. The challenge lies in the rapidly changing energy separation between the electronic states, which may span a few electron volts within a few femtoseconds in the vicinity of a CI.

Advances in attosecond science [13–18] and x-ray lasers [19–23] have opened up the possibility to observe and control processes taking place on an attosecond time scale [24–31]. In the past, ultrafast spectroscopic techniques that track the population decay or the transient change in vibration spectra have been used to study CIs [32–36]. Spontaneous emission spectroscopy [37–39] has been discussed theoretically to help visualize the intersecting electronic states, thus giving meaningful insight into the occurrence of a CI. Transient absorption [39–45] and time-resolved photoelectron [46,47] spectroscopies are, in principle, capable of observing the branching of wave packets near a CI. Time-resolved photoelectron spectroscopy [46,47] and off-resonant Raman spectroscopic methods [48,49] have been proposed to detect the presence of a coherent electronic state superposition that is created because of population transfer. One such off-resonant x-ray Raman technique is TRUECARS (transient redistribution of ultrafast electronic coherence in attosecond Raman signals) [49], which has been proposed to observe vibronic coherences present in a molecule.

A combination of 2 off-resonant pulses, called Raman probe, is used to study the vibronic coherence in the TRUECARS method. The resulting Raman signal directly shows the energy separation between the involved electronic states. The Raman probe is off-resonant with respect to the core-excited states, and thus, the signal relies on the x-ray polarizabilities of the molecule to detect the vibronic coherences. The electronic and vibrational coherences constitute the vibronic coherences present in a molecule. The strength of the signal stemming from the vibrational coherences depends on the populations of the valence states, along with the polarizability. On the other hand, the strength of the signal corresponding to the electronic coherence depends on the nuclear wave function overlap of the involved electronic states, along with the polarizabilities. For a nonstationary wave packet in an excited state, the vibrational coherences are inevitably present in a molecule and are much stronger than the electronic coherence [50]. This results in a spectrum where the vibrational contributions, created by the pump–pulse, can be larger than the electronic coherences created by the CI. Apart from containing contributions from vibrational coherences, the unmodified TRUECARS technique can only track the electronic state separation after the CI, not before the CI.

In this paper, we propose using an additional resonant pulse to create a coherent superposition between the electronic states
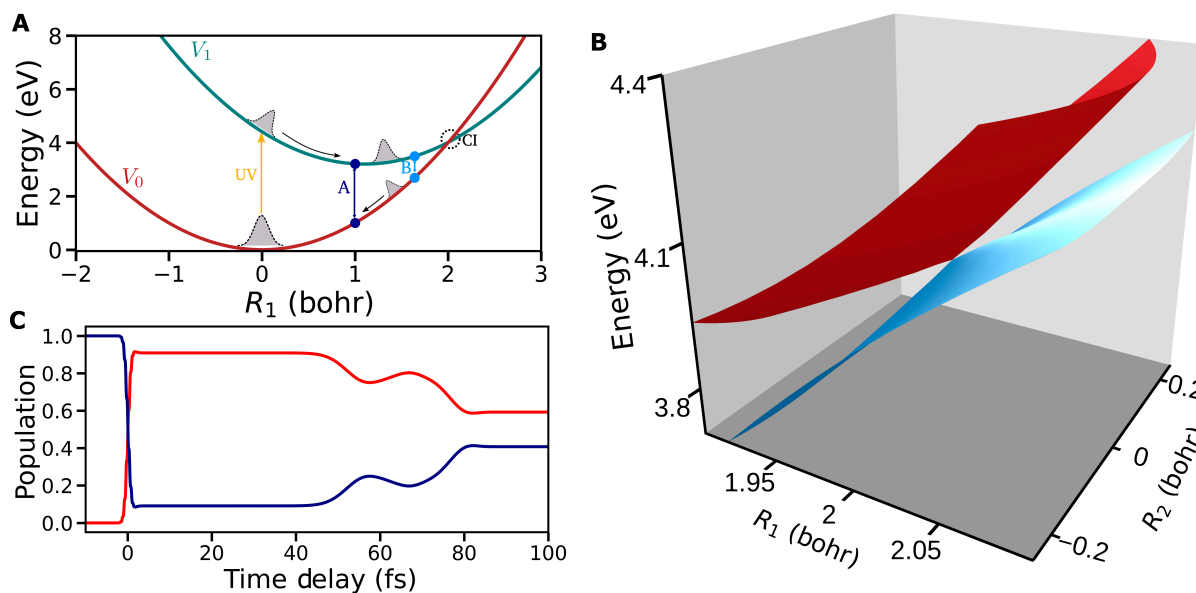
Fig. 1. Overview of the model system. (A) One-dimensional slices of the PESs along the R_1 reaction coordinate are shown. The black dashed circle shows the point of degeneracy between the two electronic states. Vertical arrows indicate transitions between the electronic states. Transition A corresponds to an electronic state separation of ≈ 2.2 eV, and transition B corresponds to an electronic state separation of ≈ 0.8 eV. (B) Two-dimensional representation of the adiabatic PESs for the electronic states involved in the CI. (C) The population dynamics of the V_0 state (blue) and V_1 state (red). The time delay axis is referenced with respect to the pump–pulse interaction.

before the measurement with a Raman probe. The artificially created superposition will allow us to gain additional information about the electronic state separation before the wave packet reaches the CI. The resulting signal is free from vibrational coherences. We theoretically demonstrate the proposed technique with a CI in a model system and explore combinations of dump–pulse and Raman probe parameters that can give a deeper insight into the nonadiabatic dynamics near the CI. Recently, a similar approach of using resonant infrared fields to enhance the features of coherences in x-ray diffraction has been demonstrated theoretically [51].

Methods

Model system with a CI

To demonstrate the proposed technique for the study of nonadiabatic dynamics in a molecule, a model system with 2 electronic states exhibiting a sloped CI is designed. The electronic states in the considered system are 2-dimensional diabatic potential energy surfaces (PESs) that are coupled with diabatic couplings in the region of the CI. One-dimensional slices of the diabatic PESs of the 2 electronic states along the R_1 reaction coordinate are shown in Fig. 1A. Analytic expressions that were used to construct the diabatic PESs and the diabatic couplings between the electronic states can be found in the Supplementary Materials. The diabatic couplings between the electronic states are constructed such that the diabatic-to-adiabatic transformation of the PES results in 2 adiabatic electronic states with a CI, as shown in Fig. 1B. The adiabatic separation between the electronic states decreases while approaching the CI and vanishes at the CI (see Fig. S1).

A UV pulse initiates the dynamics by transferring $\approx 90\%$ of the V_0 state population to the V_1 state. The population dynamics of the electronic valence states are plotted in Fig. 1C. The wave packets evolve on the V_1 state until they reach the CI region around at $R_1 = 2$ bohr, and the population transfer

between states V_1 and V_0 sets in around ≈ 50 fs. The branched wave packets move in the vicinity of the CI between 50 and 80 fs, and the system encounters 3 instances of population transfer between the electronic states during that period. In the first and third instances of the passage through the CI, 16% and 21% of the total population transfers from the V_1 state to V_0 state, respectively. During the second pass over the CI, $\approx 5\%$ of the total population is transferred from the V_0 state to V_1 state. The details of the quantum dynamics simulation can be found in the Supplementary Materials.

Spectroscopic technique

The Hamiltonian of the molecular system reads:

$$\hat{H}_1 = \hat{H}_0 + \hat{H}_P \quad (1)$$

with $\hat{H}_0$ being the bare molecular Hamiltonian for the valence states and $\hat{H}_P$ being the Hamiltonian corresponding to the pump–pulse interaction with the molecular system. The bare-molecule Hamiltonian is given by,

$$\hat{H}_0 = \begin{bmatrix} \hat{T} + \hat{V}_0 & \hat{C}_{01} \\ \hat{C}_{01} & \hat{T} + \hat{V}_1 \end{bmatrix} \quad (2)$$

where $\hat{T} = \left(-\hbar^2 / 2m_r \right) \nabla^2$ is the kinetic energy operator, with ∇ being the gradient operator with respect to the reaction coordinates R_1 and R_2; m_r is the reduced mass of the nuclei; $\hat{V}$s are the PESs of the electronic states; and $\hat{C}_{01}$ is the diabatic coupling between the 2 valence states and is an operator in the nuclear subspace. The pump–pulse Hamiltonian is given by,

$$\hat{H}_P = -\tilde{\mathcal{E}}_P \begin{bmatrix} 0 & \hat{\mu}_{01} \\ \hat{\mu}_{01} & 0 \end{bmatrix} \quad (3)$$

with $\tilde{\mathcal{E}}_P = A_0 \cos\left(\omega_P t\right) \exp\left(-t^2 / 2\sigma_P^2\right)$ being the electric field with amplitude $A_0 = 15.43$ GV/m, width $\sigma_P = 1$ fs, and center
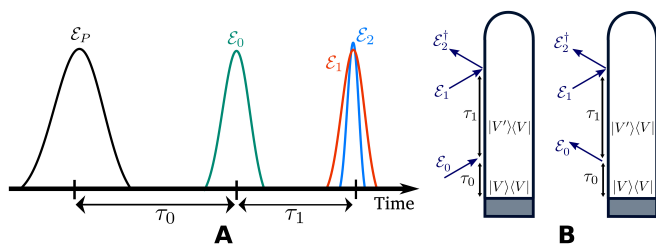
Fig. 2. (A) The pulse scheme and (B) the loop diagrams corresponding to the spectroscopic method are shown here. The gray region defines the system prepared using a pump–pulse, and $|V\rangle$ and $|V'\rangle$ indicate the electronic states. A discussion on diagrammatic construction rules and their connection with correlation functions can be found in the study of Biggs et al. [52].

frequency $\omega_P = 4.4$ eV$/\hbar$, and $\hat{\mu}_{01}$ is the transition dipole operator corresponding to the transition between V_0 and V_1 states. The system is in the vibrational and electronic ground state initially, and the pump–pulse is used to prepare the system and to initiate the nuclear dynamics.

To study the passage of the nuclear wave packet through the CI, the model system interacts with the dump–pulse, which creates a coherent superposition of the states V_1 and V_0. The coherent superposition of the electronic states that is created using the dump–pulse is probed using a Raman probe. The off-resonant Raman probe, consisting of 2 fields ($\mathcal{E}_1$ and $\mathcal{E}_2$), interacts with the system to drive transitions between the electronic states V_0 and V_1. Interactions of the excited molecule with the dump–pulse and the Raman probe–pulse are treated with time-dependent perturbation theory in the following. The total Hamiltonian of the process takes the following form,

$$\hat{H}(t) = \hat{H}_1 + \hat{H}_{int}(t) \tag{4}$$

with $\hat{H}_{int}$ being the light–matter interaction Hamiltonian considering interactions of the molecular system with all light fields except $\mathcal{E}_P$. The interaction Hamiltonian $\hat{H}_{int}$ is expressed in the interaction picture:

$$\hat{H}_{int}(t) = \left(\mathcal{E}_0(t) + \mathcal{E}_0^*(t)\right)\left(\hat{\mu}_{01}^\dagger(t) + \hat{\mu}_{01}(t)\right) \\ + \hat{\alpha}(t)\left[\mathcal{E}_2^*(t)\mathcal{E}_1(t) + \mathcal{E}_2(t)\mathcal{E}_1^*(t)\right] \tag{5}$$

where, $\mathcal{E}_0(t)$ is the dump–pulse, $\hat{\mu}_{01}$ is the operator corresponding to the transition dipole moment between the valence states, $\hat{\alpha}$ is the polarizability operator, and $\mathcal{E}_1(t)$ and $\mathcal{E}_2(t)$ are the electric fields in the Raman probe. The signal is defined as the integrated rate of change in the photon number of the $\mathcal{E}_2$ field [53],

$$S = \int \frac{d}{dt}\langle \hat{N}_{2,s}(t)\rangle dt \tag{6}$$

where $\hat{N}_{2,s} = \hat{a}_{2,s}^\dagger \hat{a}_{2,s}$ is the photon number operator corresponding to the sth mode of the field $\hat{\mathcal{E}}_2$. It is a heterodyne-detected signal, and the $\mathcal{E}_2$ pulse is recorded after its interaction with the molecule under study. Here, the expectation value in Eq. 6 corresponds to the joint field–matter wave function. The final signal expression reads,

$$S(\omega_R, \tau_1, \omega_0, \tau_0) = \frac{4}{\hbar^2}\Im \int_{-\infty}^{\infty} dt\, e^{i\omega_R(t-\tau_1)} \tilde{\mathcal{E}}_2^*(\omega_R)\tilde{\mathcal{E}}_1(t-\tau_1) \times \\ \Im \int_{-\infty}^{t} dt'\, \tilde{\mathcal{E}}_0(t'-\tau_0)\cos\left(\omega_0(t'-\tau_0)\right)C_f(t,t') \tag{7}$$

where ω_R is the Raman frequency; $\tilde{\mathcal{E}}_1$ and $\tilde{\mathcal{E}}_2$ are the envelopes of the electric field in the Raman probe with delay τ_1; $\tilde{\mathcal{E}}_0$ is the envelope of the dump–pulse; ω_0 and τ_0 are the frequency and the time delay of the dump–pulse, respectively; and C_f represents the correlation function,

$$C_f(t,t') = \left\langle \psi_0 \left| \hat{\alpha}(t)\left[\hat{\mu}_{01}^\dagger(t') + \hat{\mu}_{01}(t')\right]\right|\psi_0 \right\rangle \tag{8}$$

where Ψ_0 is the combined nuclear–electronic wave function at initial time $t = 0$, which evolves according to the Hamiltonian $\hat{H}_1$. The loop diagrams corresponding to the correlation function in Eq. 8 are shown in Fig. 2B.

As can be seen in Eq. 8, the signal depends on the strength of molecular properties, i.e., x-ray polarizability α and the transition dipole moments μ_{01}. It is essential to have nonvanishing molecular properties for the proposed method to work, especially in the CI region. The proposed method can be used to gain further insights into the nonadiabatic dynamics in molecules, such as, NO_2 [54] and LiF [55], which have allowed dipole transitions between the electronic states exhibiting CIs or avoided crossings. In the system under study, we have considered the molecular properties to be constant with respect to the reaction coordinates, R_1 and R_2. Under this assumption, the strength of the molecular properties along with the electric field intensities can be grouped in a constant factor to Eq. 7.

The signal expression in Eq. 7 depends on the dump–pulse parameters and the parameters of the Raman pulse, and hence, multidimensional signals can be constructed by varying different combinations of parameters. Note that the signal in Eq. 7 is antisymmetric with respect to ω_R and, thus, vanishes when integrated over. To reduce the number of variables, one can integrate over the positive Raman frequencies. The following expression is used for the construction of spectra that are to be displayed without frequency resolution in ω_R:

$$S'(\tau_1, \omega_0, \tau_0) = \int_0^{\infty} d\omega_R S(\omega_R, \tau_1, \omega_0, \tau_0). \tag{9}$$

By fixing 1 or 2 variables in Eq. 9, one can write 3 different versions of the signal: (a) $S'(\tau_1; \omega_0, \tau_0)$ and (b) $S'(\tau_1, \tau_0; \omega_0)$. A third version can be obtained by Fourier transforming τ_1 (c):

$$S''(\omega_1, \tau_0; \omega_0) = \left|\int_{-\infty}^{\infty} d\tau_1 e^{-i\omega_1\tau_1} S'(\tau_1, \tau_0; \omega_0)\right| \tag{10}$$

The first signal, (a) $S'(\tau_1; \omega_0, \tau_0)$, fixes the dump–pulse parameters and varies the Raman probe delay. It contains information about the time evolution of the coherent superposition created by the dump–pulse at a specific resonance between V_0 and V_1. The second signal, (b) $S'(\tau_1, \tau_0; \omega_0)$, varies both delays τ_0 and τ_1. In addition to (a), the signal provides information about the time interval for which the electronic states are resonant with the dump–pulse. The third version, (c) $S''(\omega_1, \tau_0; \omega_0)$, is a Fourier-transformed version of (b). The oscillations along τ_1 directly contain the information about the energy separation between states V_0 and V_1.

Results and Discussion

We begin with discussing the signal of type (a), $S'(\tau_1; \omega_0, \tau_0)$, where the Raman probe delay is varied, and all other variables are kept fixed. Figure 3A shows the signal that is constructed when the dump–pulse with a center frequency of 2.2 eV interacts with the system at $\tau_0 = 30$ fs. An oscillatory signal appears
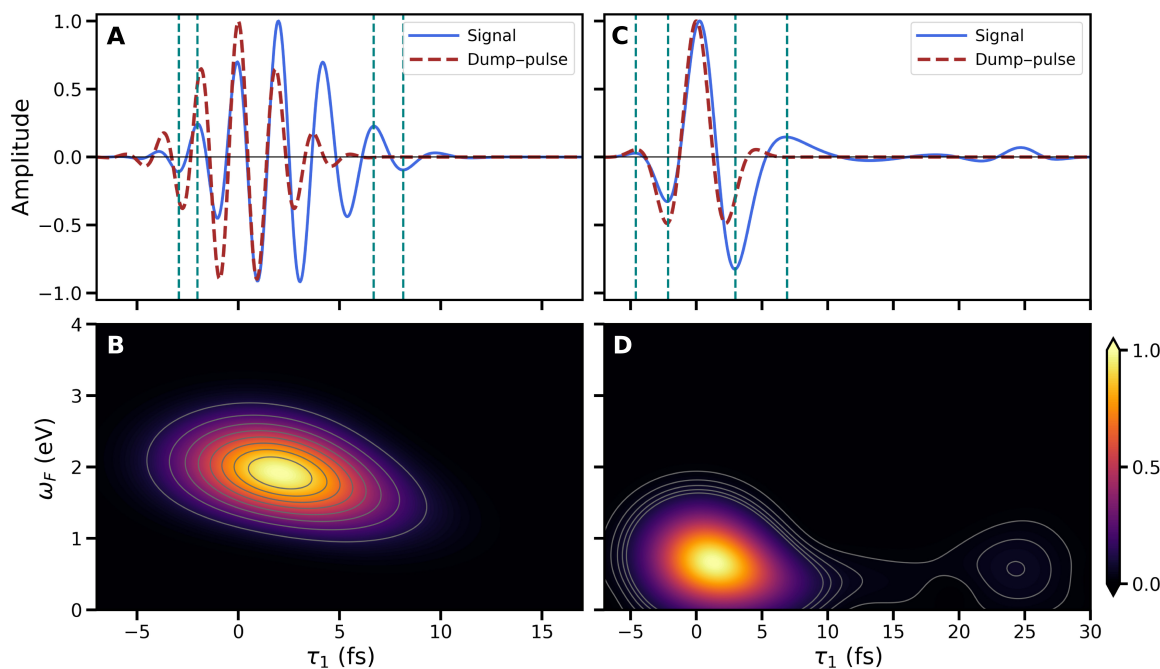
Fig. 3. Type (a) Raman and SWiFT signals for fixed dump–pulse delays: (A) Raman signal for dump–pulse delay $\tau_0 = 30$ fs and the frequency $\omega_0 = 2.2$ eV (resonant with transition A in Fig. 1A). (C) Raman signal for dump–pulse delay $\tau_0 = 43$ fs and the frequency $\omega_0 = 0.8$ eV (resonant with transition B in Fig. 1A). The vertical dashed lines mark the half-period of oscillations in the signal. The persistence of the signal after the dump–pulse vanishes represents the lifetime of the wave function overlap created because of the dump–pulse interaction. (B and D) SWiFT spectra for signals in (A) and (C), respectively, constructed using a window function with $\sigma_F = 2$ fs. The other parameters of the dump–pulse and the Raman probe are $\sigma_0 = 2$ fs, $\sigma_1 = 0.5$ fs, and $\sigma_2 = 0.5$ fs.

when the dump–pulse interacts with the molecule. The signal is in phase with the dump–pulse and originates from the coherence, created by the dump–pulse via stimulated emission, between the states V_1 and V_0. The period of oscillations in the signal corresponds to the separation between the electronic states. The signal persists for ≈ 5 fs after the dump–pulse vanishes. The decrease in the signal intensity indicates a vanishing nuclear wave function overlap caused by the different gradients in V_0 and V_1. Two pairs of vertical dashed lines in the spectrum indicate the half-period of oscillation. The observed increase in the period of oscillations indicates a decrease in the separation between the states V_1 and V_0. In order to visualize the evolving electronic state separation embedded in the Raman signal in Fig. 3A, a sliding window Fourier transform (SWiFT) spectrum can be constructed. A SWiFT spectrum can be calculated using the following expression:

$$S_F\left(\tau_F,\omega_F\right) = \left| \int_{-\infty}^{\infty} d\tau_1 e^{-i\omega_F\tau_1} e^{-(\tau_1-\tau_F)^2/2\sigma_F^2} S_a'\left(\tau_1;\omega_0,\tau_0\right) \right|$$

(11)

where τ_F is the delay of the window function, σ_F is the width of the Gaussian window function, and S_a' is the analytical signal of S' obtained using the Hilbert transform,

$$S_a' = \mathcal{F}^{-1}\left\{2\mathcal{F}\left\{S'\right\}U\right\}$$

(12)

where $\mathcal{F}$ represents the Fourier transform, and U represents a unit step function. Figure 3B shows the SWiFT spectrum constructed using Eqs. 11 and 12. The signal appears around $\omega_F = 2$ eV and moves toward lower energies with the increase in the window function delay. Therefore, the evolution of energy separation between 2 states can be tracked using type (a) Raman signals.
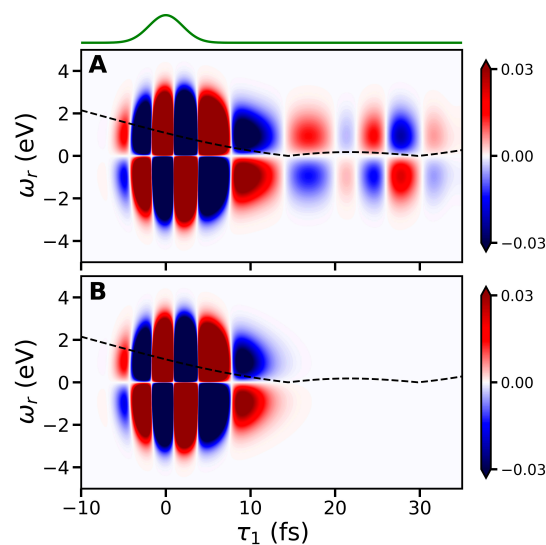

Fig. 4. Frequency-dispersed Raman signals for the dump–pulse delay $\tau_0 = 40$ fs and the frequency $\omega_0 = 0.8$ eV (resonant with transition A in Fig. 1A). (A) The signal for electronic states coupled via a CI. (B) The signal for decoupled electronic states. The intensity axes are rescaled to 3% of the maximum intensity of the respective signals. The black dashed curve shows the time-varying electronic state separation approximated using the wave functions in the V_1 state. The green curve shows the dump–pulse envelope. The other parameters of the dump–pulse and the Raman probe are $\sigma_0 = 2$ fs, $\sigma_1 = 0.5$ fs, and $\sigma_2 = 0.5$ fs.

Figure 3B shows the signal generated by the interaction of the system with the dump–pulse, with $\omega_0 = 0.8$ eV at $\tau_0 = 43$ fs. The signal here is short-lived and approximately follows the field of the dump–pulse and nearly vanishes by $\tau_1 \approx 10$ fs. A weak signal persists until $\tau_1 = 30$ fs because of the motion
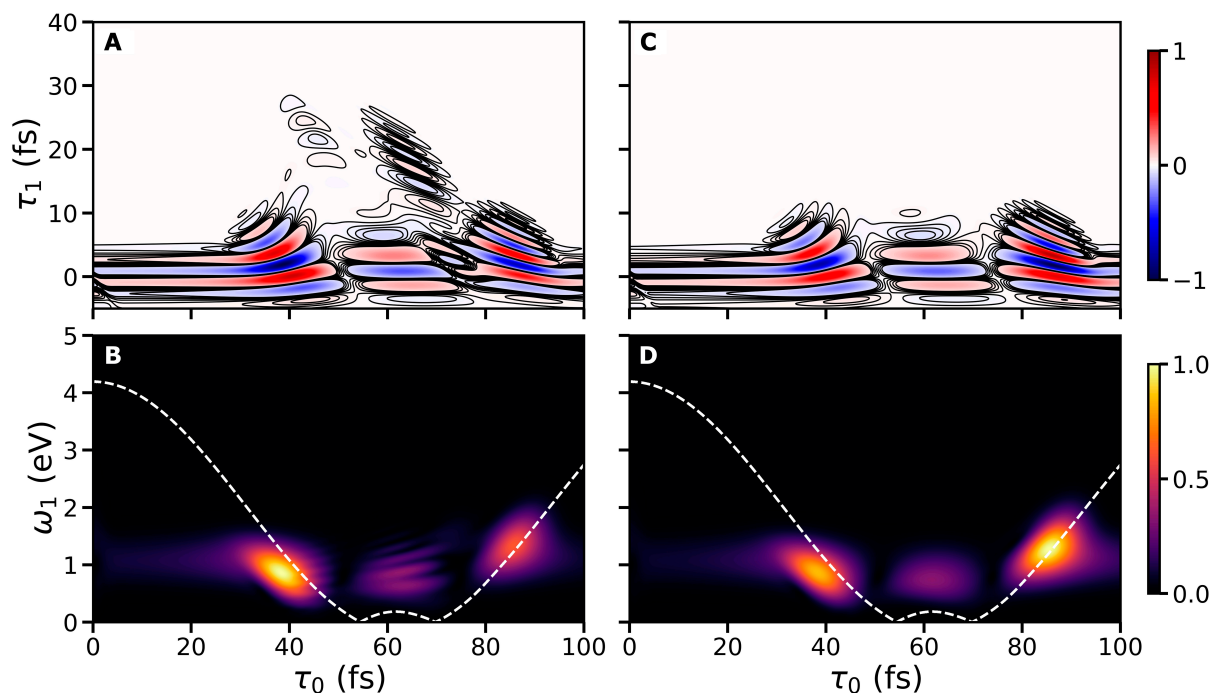
Fig. 5. Two-dimensional Raman signals for (A and B) coupled and (C and D) decoupled electronic states. (A and C) Signals of type (b) show the time interval during which the system is resonant with the dump–pulse frequency along the τ_0 axis, whereas the decay of the wave function overlap appears along the τ_1 axis. (B and D) Signals of type (c) are shown here, along with the white dashed curve showing the time-varying electronic state separation approximated using the wave functions in the V_1 state. The other parameters of the dump–pulse and the Raman probe are $\sigma_0 = 2$ fs, $\omega_0 = 1$ eV, $\sigma_1 = 0.5$ fs, and $\sigma_2 = 0.5$ fs.

of wave packets in the CI region. A SWiFT spectrum is constructed for the Raman signal in Fig. 3C to visualize the evolving electronic state separation and is shown in Fig. 3D. The signal is localized below 1 eV and does not decay entirely after the dump–pulse vanishes. A revival of the signal at $\tau_1(\tau_F) \approx 25$ fs (corresponding to 68 fs in Fig. 1C) in Fig. 3C and D appears because of the recrossing of the wave packets through the CI.

To demonstrate the interplay of the coherence generated by the dump–pulse and the CI, we construct frequency-dispersed Raman signals ($S(\omega_R, \tau_1; \omega_0 = 0.8$ eV, $\tau_0 = 40$ fs); Eq. 7) for the model system with and without diabatic couplings. There is no population transfer near the intersection of the electronic states when the diabatic couplings are removed from the model system shown in Fig. 1A. Figure 4A and B shows the Raman signals for the system with and without coupled electronic states, respectively. The Raman gain–loss features can be observed in both spectra when the dump–pulse (green curve) is applied. The signals here are similar to a TRUECARS signal, except that the coherence has been created by a laser pulse instead of the CI. The black dashed curve shows an approximate time-dependent electronic state separation curve to track the intersection of the electronic states (see Eq. S18). Note that the approximate electronic state separation curve is obtained using nuclear wave functions of the V_1 state and is only applicable when the wave packets are localized on the PESs near and before the CI. The signal intensities drop substantially after the dump–pulse vanishes, but a weak signal appears in Fig. 4A until after 30 fs, which is missing in Fig. 4B. The appearance of the signal in Fig. 4A after ≈15 fs can be attributed to the revival of the coherence generated by the dump–pulse, after the CI when the black dashed curve touches $\omega_r = 0$ eV. When the dump–pulse-generated coherence goes through the CI, it gives rise to

a new coherence in which the wave packets are antisymmetric about R_2. This phenomenon is denoted as the revival of the dump–pulse-generated coherence due to the passage through the CI. The 3 consecutive passages through the CI give rise to multiple coherences that interfere with each other. Hence, the period of oscillations in Fig. 4A after the CI does not clearly represent the electronic state separation (black dashed curve). Note that only the intrinsically generated coherence cannot be observed directly in our system because of the symmetric nature of the polarizability and antisymmetric nature of the diabatic couplings. Therefore, studying the evolution of the coherence created by the dump–pulse may help track the occurrence of a CI even if the intrinsic electronic coherence cannot be observed because of symmetry constraints or restrictions in Raman selection rules.

To study the decoherence time of the electronic superposition and to map the time-varying electronic state separation, we construct the full 2-dimensional signals of type (b) and (c) by varying both delays τ_0 and τ_1. We construct 2-dimensional spectra for the model system with and without the coupled electronic states to study the significance of the CI. The resulting spectra are shown in Fig. 5. Distinct signals appear after $\tau_0 = 30$ fs in Fig. 5A and C when the wave packets arrive in the region that is resonant with the dump–pulse frequency. Along the τ_0 axis, the phase of signals in Fig. 5A and C changes by 180° after ≈50 fs when the wave packet crosses through the intersection, which indicates a change from the stimulated emission to the absorption of the dump–pulse photons. A similar phase change appears around $\tau_0 = 80$ fs when the wave packets go through the intersection region again. Between $\tau_0 = 50$ and 80 fs, a nonvanishing signal appears above $\tau_1 = 10$ fs in Fig. 5A, which is missing in Fig. 5C. Between $\tau_0 = 50$ and 80 fs in Fig. 5A, the decoherence time is longer than 20 fs

and starts to decrease again after 80 fs. The extended lifetime of the coherence in Fig. 5A can be attributed to the revival of the coherence because of the generation of new coherences after each passage through the CI.

The information about the evolving electronic state separation can be obtained by Fourier transforming the τ_1 axis for Fig. 5A and C, as shown in Fig. 5B and D, respectively. In Fig. 5B and D, a strong signal emerges after 30 fs that follows the white dashed curve, which shows the changing electronic state separation with time. A vanishing signal that appears around 50 and 75 fs in Fig. 5B and D corresponds to the time interval when the phase of the signal switches along the τ_0 axes in Fig. 5A and C. The increasing electronic state separation can be seen after 80 fs when the wave packets move away from the intersection region in both signals. Spectra in Fig. 5B and D differ in the CI region where there are oscillations below 1 eV in Fig. 5B, which are absent in Fig. 5D. After the passage through the CI, the spectrum that follows the white dashed curve in Fig. 5B faces a dip in intensity compared to before the CI. Such a decrease in the intensity is not observed in Fig. 5B. Spectra similar to Fig. 5B with several dump–pulse frequencies can be used to trace out the entire dynamics and are available in the Supplementary Materials. Therefore, the use of few femtoseconds-short dump–pulses with a fixed center frequency to construct a spectrum with τ_0 and τ_1 as parameters may help track the changing electronic state separation with time along with visualizing the lifetime of the artificial coherence near and far from the CI.

Conclusion

We have presented a nonlinear, 2-dimensional, Raman technique that is studied using a CI in a molecular model system. The proposed technique can be viewed as an extension to the TRUECARS technique, which adds a dump–pulse to the scheme. We have explored different combinations of dump–pulse and Raman probe parameters to investigate the signatures of the CI. We could demonstrate that this technique carries information about the vibronic coherences created in the vicinity of the CI and the dynamic electronic state separation before and after the CI. The investigated signals are not sensitive to intrinsic vibrational coherences as they are, for example, created by the UV pump–pulse. The presented 2-dimensional spectra containing 2 main pieces of information, namely, the time-varying energy separation between the electronic states and the lifetimes of the created electronic coherences. These lifetimes can be read from the spectrum easily and are connected to the gradient difference of the involved electronic states, along with the nonadiabatic dynamics near CI.

This technique is an enhancement of the TRUECARS technique in the following ways: (a) The region before the nuclear wave packet that reaches the CI can now also be explored. (b) The insensitivity of the signal to preexisting vibrational coherences increases the contrast of the Raman probe. (c) The signal contains information of the coherences created in the vicinity of the CI, even if their TRUECARS signature vanishes because of Raman selection rules.

Acknowledgments

Data Availability

The data that support the findings of this study are available from the corresponding author upon reasonable request.

Supplementary Materials

Figs. S1 to S6.

References

1. Polli D, Altoè P, Weingart O, Spillane KM, Manzoni C, Brida D, Tomasello G, Orlandi G, Kukura P, Mathies RA, et al. Conical intersection dynamics of the primary photoisomerization event in vision. *Nature*. 2010;467(7314):440–443.

2. Sinha RP, Häder D-P. UV-induced DNA damage and repair: A review. *Photochem Photobiol Sci*. 2002;1(4):225–236.

3. Yarkony DR. Conical intersections: Diabolical and often misunderstood. *Acc Chem Res*. 1998;31(8):511–518.

4. Matsika S, Krause P. Nonadiabatic events and conical intersections. *Annu Rev Phys Chem*. 2011;62:621–643.

5. Domcke W, Yarkony D, Köppel H. *Conical intersections: Electronic structure, dynamics & spectroscopy*. Singapore: World Scientific; 2004. p. 15.

6. Baer M. *Beyond Born-Oppenheimer: Electronic nonadiabatic coupling terms and conical intersections*. New Jersey (USA): John Wiley & Sons; 2006.

7. Domcke W, Yarkony DR, Köppel H. *Conical intersections*. Singapore: World Scientific; 2011.

8. Combes J-M, Duclos P, Seiler R. *Rigorous atomic and molecular physics*. Boston (USA): Springer; 1981. p. 185–213.

9. Woolley RG, Sutcliffe BT. Molecular structure and the Born–Oppenheimer approximation. *Chem Phys Lett*. 1977;45:393–398.

10. Essén H. The physics of the Born–Oppenheimer approximation. *Int J Quantum Chem*. 1977;12(4):721–735.

11. Cederbaum LS. Born–Oppenheimer approximation and beyond for time-dependent electronic processes. *J Chem Phys*. 2008;128(12):124101.

12. Robb MA. In this molecule there must be a conical intersection. *Adv Phys Org Chem*. 2014;48:189–228.

13. Zhang C-H, Thumm U. Attosecond photoelectron spectroscopy of metal surfaces. *Phys Rev Lett*. 2009;102(12):123601.

14. Calegari F, Ayuso D, Trabattoni A, Belshaw L, De Camillis S, Anumula S, Frassetto F, Poletto L, Palacios A, Decleva P, et al. Ultrafast electron dynamics in phenylalanine initiated by attosecond pulses. *Science*. 2014;346(6207):336–339.

15. Calegari, F, Sansone G, Stagira S, Vozzi C, Nisoli M. Advances in attosecond science. *J Phys B At Mol Opt Phys*. 2016;49(6):Article 062001.

16. Krausz F, Ivanov M. Attosecond physics. *Rev Mod Phys*. 2009;81(1);163.

17. Itatani J, Quéré F, Yudin GL, Ivanov MY, Krausz F, Corkum PB. Attosecond streak camera. *Phys Rev Lett*. 2002;88(17):173903.

18. Popova-Gorelova D, Küpper J, Santra R. Imaging electron dynamics with time- and angle-resolved photoelectron spectroscopy. *Phys Rev A*. 2016;94(1):Article 013412.

19. Rohringer N, Ryan D, London RA, Purvis M, Albert F, Dunn J, Bozek JD, Bostedt C, Graf A, Hill R, et al. Atomic inner-shell X-ray laser at 1.46 nanometres pumped by an X-ray free-electron laser. *Nature*. 2012;481(7382):488–491.

20. Rouxel JR, Kowalewski M, Bennett K, Mukamel S. X-ray sum frequency diffraction for direct imaging of ultrafast electron dynamics. *Phys Rev Lett*. 2018;120(24):243902.

21. Miao J, Ishikawa T, Robinson IK, Murnane MM. Beyond crystallography: Diffractive imaging using coherent x-ray light sources. *Science*. 2015;348(6234):530–535.

22. Krebs D, Rohringer N. Theory of parametric x-ray optical wavemixing processes. arXiv. 2021. https://arxiv.org/abs/2104.05838

23. Rohringer N, Santra R. X-ray nonlinear optical processes using a self-amplified spontaneous emission free-electron laser. *Phys Rev A*. 2007;76(3):Article 033416.

24. Bressler C, Chergui M. Ultrafast X-ray absorption spectroscopy. *Chem Rev*. 2004;104(4):1781–1812.

25. Galbraith MCE, Scheit S, Golubev NV, Reitsma G, Zhavoronkov N, Despré V, Lépine F, Kuleff AI, Vrakking MJJ, Kornilov O, et al. Few-femtosecond passage of conical intersections in the benzene cation. *Nat Commun*. 2017;8(1):1–7.

26. Krčmář J, Gelin MF, Egorova D, Domcke W. Signatures of conical intersections in two-dimensional electronic spectra. *J Phys B At Mol Opt Phys*. 2014;47(12):Article 124019.

27. Sala M, Egorova D. Two-dimensional photon-echo spectroscopy at a conical intersection: A two-mode pyrazine model with dissipation. *Chem Phys*. 2016;481:206–217.

28. Inhester L, Greenman L, Rudenko A, Rolles D, Santra R. Detecting coherent core-hole wave-packet dynamics in N_2 by time- and angle-resolved inner-shell photoelectron spectroscopy. *J Chem Phys*. 2019;151(5);Article 054107.

29. Sun K, Xie W, Chen L, Domcke W, Gelin MF. Multi-faceted spectroscopic mapping of ultrafast nonadiabatic dynamics near conical intersections: A computational study. *J Chem Phys*. 2020;153(17):174111.

30. Smolarek S, Rijs AM, Buma WJ, Drabbels M. Absorption spectroscopy of adenine, 9-methyladenine, and 2-aminopurine in helium nanodroplets. *Phys Chem Chem Phys*. 2010;12(48):15600–15606.

31. Hosseinizadeh A, Breckwoldt N, Fung R, Sepehr R, Schmidt M, Schwander P, Santra R, Ourmazd A. Few-fs resolution of a photoactive protein traversing a conical intersection. *Nature*. 2021;599(7886):697–701.

32. Yang J, Zhu X, Wolf TJ, Li Z, Nunes JPF, Coffee R, Cryan JP, Gühr M, Hegazy K, Heinz TF, et al. Imaging CF3I conical intersection and photodissociation dynamics with ultrafast electron diffraction. *Science*. 2018;361(6397):64–67.

33. Wörner HJ, Bertrand JB, Fabre B, Higuet J, Ruf H, Dubrouil A, Patchkovskii S, Spanner M, Mairesse Y, Blanchet V, et al. Conical intersection dynamics in NO_2 probed by homodyne high-harmonic spectroscopy. *Science*. 2011;334(6053):208–212.

34. Wolf T, Myhre RH, Cryan J, Coriani S, Squibb R, Battistoni A, Berrah N, Bostedt C, Bucksbaum P, Coslovich G, et al. Probing ultrafast $\pi\pi^*$/$n\pi^*$ internal conversion in organic chromophores via K-edge resonant absorption. *Nat Commun*. 2017;8:1–7.

35. Duan H.-G, Jha A, Li X, Tiwari V, Ye H, Nayak PK, Zhu X.-L, Li Z, Martinez TJ, Thorwart M, et al. Intermolecular vibrations mediate ultrafast singlet fission. *Sci Adv*. 2020;6(38):Article eabb0052.

36. Gessner O, Gühr M. Monitoring ultrafast chemical dynamics by time-domain x-ray photo- and auger-electron spectroscopy. *Acc Chem Res*. 2016;49(1):138–145.

37. Santoro F, Petrongolo C, Lami A. Time- and frequency-resolved spontaneous emission: Theory and application to the NO_2 $\tilde{X}^2$ $A'/\tilde{A}^2$ A' conical intersection. *J Chem Phys*. 2000;113:4073–4082.

38. Patuwo MY, Lee S-Y. Probing non-adiabatic conical intersections using absorption, spontaneous Raman, and femtosecond stimulated Raman spectroscopy. *J Chem Phys*. 2013;139:234101.

39. Jadoun D, Gudem M, Kowalewski M. Capturing fingerprints of conical intersection: Complementary information of non-adiabatic dynamics from linear x-ray probes. *Struct Dyn*. 2021;8(3):Article 034101.

40. Kobayashi Y, Chang KF, Zeng T, Neumark DM, Leone, SR. Direct mapping of curve-crossing dynamics in IBr by attosecond transient absorption spectroscopy. *Science*. 2019;365(6448):79–83.

41. Zinchenko KS, Ardana-Lamas F, Seidu I, Neville SP, van der Veen J, Lanfaloni VU, Schuurman MS, Wörner HJ. Sub-7-femtosecond conical-intersection dynamics probed at the carbon K-edge. *Science*. 2021;371(6528):489–494.

42. Oliver TA, Fleming GR. Following coupled electronic-nuclear motion through conical intersections in the ultrafast relaxation of β-Apo-8′-carotenal. *J Phys Chem B*. 2015;119(34):11428–11441.

43. Timmers H, Zhu X, Li Z, Kobayashi Y, Sabbar M, Hollstein M, Reduzzi M, Martínez TJ, Neumark DM, Leone SR. Disentangling conical intersection and coherent molecular dynamics in methyl bromide with attosecond transient absorption spectroscopy. *Nat Commun*. 2019;10:1–8.

44. Bækhøj JE, Lévêque C, Madsen LB. Signatures of a conical intersection in attosecond transient absorption spectroscopy. *Phys Rev Lett*. 2018;121(2):Article 023203.

45. Kowalewski M, Fingerhut BP, Dorfman KE, Bennett K, Mukamel S. Simulating coherent multidimensional spectroscopy of nonadiabatic molecular processes: From the infrared to the X-ray regime. *Chem Rev*. 2017;117(19):12165–12226.

46. Bennett K, Kowalewski M, Mukamel S. Nonadiabatic dynamics may be probed through electronic coherence in time-resolved photoelectron spectroscopy. *J Chem Theory Comput*. 2016;12(2):740–752.

47. Jadoun D, Kowalewski M. Time-resolved photoelectron spectroscopy of conical intersections with attosecond pulse trains. *J Phys Chem Lett*. 2021;12(33):8103–8108.

48. Dorfman KE, Bennett K, Mukamel S. Detecting electronic coherence by multidimensional broadband stimulated x-ray Raman signals. *Phys Rev A*. 2015;92(2):23826.

49. Kowalewski M, Bennett K, Dorfman KE, Mukamel S. Catching conical intersections in the act: Monitoring transient electronic coherences by attosecond stimulated X-ray Raman signals. *Phys Rev Lett*. 2015;115(19):193003.

50. Restaino L, Jadoun D, Kowalewski M. Probing nonadiabatic dynamics with attosecond pulse trains and soft x-ray Raman spectroscopy. *Struct Dyn*. 2022;9(3):Article 034101.

51. Keefer D, Rouxel JR, Aleotti F, Segatta F, Garavelli M, Mukamel S. Diffractive imaging of conical intersections amplified by resonant infrared fields. *J Am Chem Soc*. 2021;143(34):13806–13815.

52. Biggs JD, Voll JA, Mukamel S. Coherent nonlinear optical studies of elementary processes in biological complexes: Diagrammatic techniques based on the wave function versus the density matrix. *Philos Trans R Soc A*. 2012;370:3709–3727.

53. Mukamel S. *Principles of nonlinear optical spectroscopy*. New York (USA): Oxford University Press; 1999. Oxford series in optical and imaging sciences.

54. Schnappinger T, de Vivie-Riedle R. Coupled nuclear and electron dynamics in the vicinity of a conical intersection. *J Chem Phys*. 2021;154(13):134306.

55. Triana JF, Peláez D, Sanz-Vicario JL. Entangled photonic-nuclear molecular dynamics of LiF in quantum optical cavities. *J Phys Chem A*. 2018;122(8):2266–2278.